Available online at website: https://journal.bcrec.id/index.php/bcrec

Bulletin of Chemical Reaction Engineering & Catalysis, 21 (2) 2026, 349-361

Original Research Article

Effect of Nickel Incorporation on Nitrogen-Doped Titania/Zirconia Nanocomposites for Enhanced Visible-Light Photocatalytic Degradation of Phenol

Akhmad Syoufian[1,*], Aldino Javier Saviola[1], Reza Rodhatul Janah[1], Rina Afifah[1], Karna Wijaya[1], Rian Kurniawan[1], Sri Sudiono[1], Won-Chun Oh[2], Wangsa Wangsa[1]

[1]Department of Chemistry, Faculty of Mathematics and Natural Sciences, Universitas Gadjah Mada, Yogyakarta, 55281, Indonesia.
[2]Department of Advanced Materials Science and Engineering, Hanseo University, Seosan, Chungnam 356-706, Republic of Korea.

Received: 7th November 2025; Revised: 5th February 2026; Accepted: 5th February 2026
Available online: 7th February 2026; Published regularly: August 2026

Abstract

The rapid expansion of industrial activities has resulted in the discharge of persistent organic pollutants, such as phenol, into aquatic environments. Nowadays, developing visible-light-responsive photocatalysts for the efficient degradation of such pollutants remains a major environmental challenge. In this study, nickel–nitrogen co-doped titania immobilized on zirconia (Ni,N–TiO_2/ZrO_2) nanocomposites with varying nickel loadings were synthesized and evaluated for phenol photodegradation under visible-light irradiation. Nickel incorporation significantly modified the optical and photocatalytic properties of the materials. The 5% Ni,N–TiO_2/ZrO_2 catalyst exhibited the lowest band gap energy (2.69 eV) compared with N–TiO_2/ZrO_2 (3.03 eV), leading to improved visible-light absorption and enhanced charge transfer. Under the experimental conditions (initial phenol concentration = 10 mg.L^{-1}, catalyst dosage = 100 mg, irradiation time = 120 min), it achieved a phenol removal efficiency of 85.36% with an apparent rate constant of 0.0229 min^{-1}, outperforming N–TiO_2/ZrO_2 (40.72%, 0.0042 min^{-1}). These results confirm that a 5 wt% nickel loading provides the most effective modification, demonstrating a strong synergistic interaction between nickel and nitrogen that enhances photocatalytic activity. The developed Ni,N–TiO_2/ZrO_2 catalyst, therefore, holds significant promise for future applications in water purification and environmental remediation.

Keywords: Advanced oxidation process; environmental remediation; photocatalysis; titania; zirconia

How to Cite: Syoufian, A., Saviola, A. J., Janah, R. R., Afifah, R., Wijaya, K., Kurniawan, R., Sudiono, S., Oh, W., Wangsa, W. (2026). Effect of Nickel Incorporation on Nitrogen-Doped Titania/Zirconia Nanocomposites for Enhanced Visible-Light Photocatalytic Degradation of Phenol. *Bulletin of Chemical Reaction Engineering & Catalysis*, 21 (2), 349-361. (DOI: 10.9767/bcrec.20529)

Permalink/DOI: https://doi.org/10.9767/bcrec.20529

1. Introduction

Water pollution has become one of the most critical global environmental challenges, driven by rapid population growth, industrial expansion, and urbanization, which together increase both water demand and pollutant discharge [1]. Among various organic pollutants, phenolic compounds are of particular concern due to their widespread industrial use and high toxicity. Each year, more than 10 million tons of phenolic compounds are released into the environment from petrochemical, pharmaceutical, textile, and agrochemical industries [2,3]. Even at low concentrations (10–24 mg.L^{-1}), phenol can irritate the skin, eyes, and mucous membranes, while prolonged exposure may lead to neurological and systemic disorders [4,5]. Therefore, developing efficient methods for phenol removal from wastewater is essential. However, conventional treatment techniques such as distillation, membrane filtration, adsorption, and biological

* Corresponding Author.
Email: akhmadsyoufian@ugm.ac.id (A. Syoufian)

degradation often face limitations including high operational costs, incomplete mineralization, and poor scalability [6–8].

In recent years, photocatalysis has emerged as a highly effective and sustainable method for degrading recalcitrant organic pollutants. This process relies on the generation of reactive oxygen species (ROS) under light irradiation, leading to the complete mineralization of contaminants into harmless products [9,10]. Titanium dioxide (TiO_2) remains one of the most studied photocatalysts owing to its low cost, high stability, and environmental compatibility [11,12]. However, its photocatalytic activity is primarily restricted to the ultraviolet (UV) region due to its wide band gap (~3.2 eV for anatase), while UV light accounts for only about 4–5% of the solar spectrum [13].

To address this limitation, zirconium dioxide (ZrO_2) has been introduced as a support material for TiO_2. The ZrO_2 offers high thermal and chemical stability and strong electron-trapping capability, which together enhance charge-carrier separation and improve photocatalytic performance. Moreover, ZrO_2 effectively inhibits the anatase-to-rutile phase transformation of TiO_2 during synthesis and operation, thereby preserving the highly active anatase phase [14–17]. The integration of TiO_2 with ZrO_2 thus provides a robust and stable platform for further surface and electronic modifications aimed at improving visible-light photocatalytic efficiency.

Band gap engineering through doping has proven to be an effective strategy for extending TiO_2 activity into the visible region. Nitrogen doping introduces localized energy states near the valence band, allowing visible-light absorption and enhancing electron mobility while minimizing lattice distortion due to the comparable atomic sizes of nitrogen and oxygen [18,19]. Transition metal dopants such as Ni^{2+} can further tailor the electronic structure, promote charge transfer, and suppress electron–hole recombination, resulting in improved photocatalytic efficiency under visible-light irradiation [20,21].

Numerous TiO_2-based photocatalysts have been explored for phenol degradation under UV and visible lights. For example, Fuentes *et al.* [22] reported 50% phenol degradation after 120 min using $Fe/TiO_2–SiO_2$ under a 150 W halogen lamp (50 $mg.L^{-1}$ phenol, 1 $g.L^{-1}$ catalyst). Zhang *et al.* [23] achieved 70.0% degradation within 150 min using 5% carbon-doped TiO_2 under UV irradiation from a 300 W mercury lamp, outperforming pure TiO_2 (53.0%) under similar conditions. Li *et al.* [24] demonstrated 89.8% degradation using a 30% TiO_2/montmorillonite composite (10 $mg.L^{-1}$ phenol, pH of 6) after 240 min of UV exposure. Although these studies highlight the potential of TiO_2-based photocatalysts, most systems still depend on UV light, which limits their practical use under natural sunlight.

Despite these advancements, limited attention has been given to nickel–nitrogen co-doped titania immobilized on zirconia (Ni,N–TiO_2/ZrO_2) for visible-light-driven photocatalysis. The synergistic interaction between nickel and nitrogen dopants, combined with the structural stabilization provided by ZrO_2, is expected to enhance charge separation, extend visible-light absorption, and prevent the anatase-to-rutile phase transition. Therefore, this study investigates the effect of nickel incorporation into nitrogen-doped TiO_2/ZrO_2 nanocomposites for phenol photodegradation under visible-light irradiation. The findings provide new insights into designing structurally stable and solar-responsive photocatalysts, offering a promising pathway toward sustainable water purification technologies.

2. Materials and Method

2.1 Materials

The materials used in this study included commercial zirconia nanopowder (ZrO_2, Smart Lab), urea (CH_4N_2O, Merck), nickel(II) sulfate hexahydrate ($NiSO_4 \cdot 6H_2O$, Merck), titanium(IV) tetraisopropoxide (TTIP, Sigma-Aldrich), ethanol (C_2H_5OH, Merck), deionized water (CV Bima Aksara Nusa), and phenol (C_6H_5OH, Merck). All chemicals were of analytical grade and were used as received without further purification.

2.2. Synthesis of the Photocatalysts

Nickel–nitrogen co-doped titania/zirconia (Ni,N–TiO_2/ZrO_2) photocatalysts were synthesized via a sol–gel method. In a typical preparation, 25 mL of absolute ethanol was mixed with 2.5 mL of titanium(IV) isopropoxide (TTIP) under magnetic stirring of 450 rpm for 20 min at room temperature to obtain a homogeneous titanium precursor solution.

Separately, an aqueous solution containing nickel precursor salts (0, 1, 3, 5, and 7 wt% Ni relative to Ti), urea (10 wt% relative to Ti), and commercial ZrO_2 powder (1 g) was dispersed in 25 mL of deionized water. The aqueous suspension was added dropwise (1 $mL.min^{-1}$) to the Ti precursor solution under continuous stirring to initiate hydrolysis and condensation of TTIP in the presence of the dispersed ZrO_2 particles. The initial pH of the mixed sol was approximately 6–7, and no additional pH adjustment was applied. Gelation occurred gradually within 30 min, as indicated by a marked increase in viscosity and formation of a homogeneous gel. During this process, TiO_2 species nucleated and grew around the ZrO_2 particles, enabling intimate interfacial contact and uniform dispersion of ZrO_2 throughout the TiO_2 matrix rather than simple post-synthesis physical mixing.

After complete gelation, the mixture was stirred for an additional 30 min to ensure homogeneity, followed by centrifugation at 3000 rpm for 30 min. The recovered gel was air-dried at room temperature for 24 h with intermittent grinding to obtain a fine powder and subsequently heated at 80 °C for 24 h to remove residual solvents. Finally, the dried materials were calcined at 500 °C for 4 h in a muffle furnace with a heating rate of 10 °C.min^{-1} to induce crystallization, remove residual organics, and facilitate dopant incorporation, where urea decomposition generates reactive nitrogen species for N-doping and nickel precursors are converted into Ni–O species that integrate into the TiO_2 framework. The obtained samples were denoted as N–TiO_2/ZrO_2, 1% Ni–N–TiO_2/ZrO_2, 3% Ni–N–TiO_2/ZrO_2, 5% Ni–N–TiO_2/ZrO_2, and 7% Ni–N–TiO_2/ZrO_2, corresponding to their respective nickel loadings. A schematic illustration of the synthesis process is shown in Figure 1.

2.3. Characterization of the Photocatalysts

The crystalline phases of the synthesized photocatalysts were analyzed using an X-ray diffractometer (XRD, D8 Advance, Bruker) equipped with Cu-Kα radiation (λ = 1.54 Å). The average crystallite size (D) was calculated using the Scherrer equation (Equation (1)), where k = 0.94, λ = 0.154 nm, β is the full width at half maximum (FWHM) in radians, and θ is the Bragg angle.

$$D = \frac{k\,\lambda}{\beta \cos\theta} \quad (1)$$

The functional groups of the samples were identified by Fourier transform infrared spectroscopy (FTIR, Shimadzu Prestige-21) using the KBr pellet method. Optical properties were evaluated with a diffuse reflectance UV–visible spectrophotometer (DRUV–Vis, Jasco V-760). Surface morphology and elemental composition were examined using a scanning electron microscope equipped with an energy-dispersive X-ray spectrometer (SEM–EDX, JEOL JED-2300).

2.4. Photocatalytic Activity Tests

The photocatalytic performance of the synthesized materials was evaluated by phenol degradation under visible-light irradiation. In each experiment, 100 mg of photocatalyst was dispersed in 100 mL of a 10 mg.L^{-1} phenol solution. The suspension was magnetically stirred, and visible-light irradiation was applied for 15, 30, 45, 60, 75, 90, 105, and 120 min using a Philips TL-D 30W/54–765 fluorescent lamp as the light source, under continuous stirring.

Adsorption experiments in the dark were not performed, as the objective of this work was to evaluate the overall photocatalytic activity of the nanocomposites under visible-light irradiation, during which adsorption and photocatalytic degradation occur simultaneously. After irradiation, the photocatalyst was separated by centrifugation at 3000 rpm for 30 min, and the residual phenol concentration was determined using a UV–Vis spectrophotometer at 269 nm. The photocatalytic degradation kinetics were analyzed using the Langmuir–Hinshelwood (L–H) model (Equation (2)), where k_r is the surface reaction rate constant. At low reactant concentrations, the equation simplifies to Equation (3), where k_{obs} is the apparent rate constant, C is the phenol concentration at time t, and C_0 is the initial phenol concentration. The phenol removal efficiency (%) was calculated using Equation (4), where C_i and C_f represent the initial and final phenol concentrations, respectively.

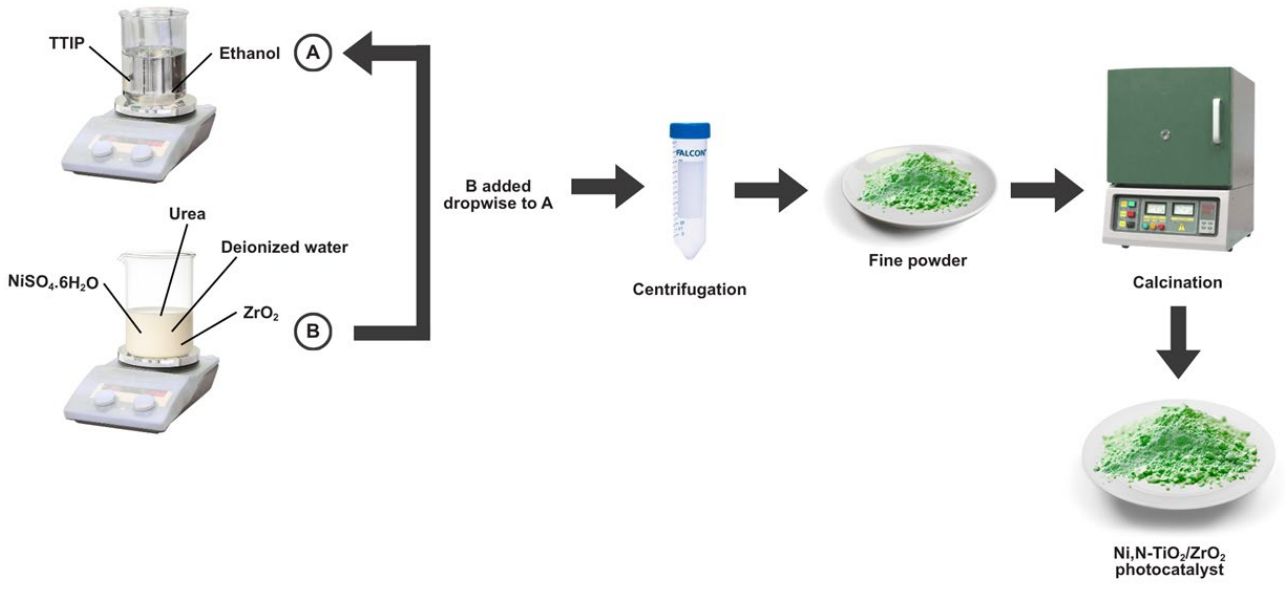

Figure 1. Schematic diagram of the photocatalyst synthesis procedure used in this study.

$$r = \frac{k_r K_L C}{1 + K_L C} \quad (2)$$

$$\ln \frac{C}{C_0} = -k_r K_L t = -k_{obs} t \quad (3)$$

$$Phenol\ removal\ efficiency\ (\%) = \frac{C_i - C_f}{C_i} \times 100\% \quad (4)$$

3. Results and Discussion

3.1. X-ray Diffraction Analysis

Figure 2 shows the XRD patterns of the photocatalysts with varying Ni co-dopant concentrations. The characteristic diffraction peaks of anatase TiO_2 appear at 2θ values of 25.44° and 54.99°, consistent with JCPDS No. 01-073-1764 [25], while peaks at 30.07° and 50.22° correspond to the tetragonal ZrO_2 phase (JCPDS No. 01-079-1767). The absence of peak shifts in the tetragonal ZrO_2 phase with increasing Ni loading indicates that the ZrO_2 lattice remains structurally and chemically stable. This stability is advantageous because it suppresses the anatase-to-rutile phase transformation in TiO_2, thereby preserving the photocatalytically active anatase phase within the nanocomposite.

Crystallite sizes were estimated using the Scherrer equation based on the full width at half maximum (FWHM) of the most intense diffraction peak of each phase, namely the anatase TiO_2 (101) and tetragonal ZrO_2 (101) reflections, to ensure consistent and reliable comparison among all samples (Table 1). For the anatase (101) plane, the undoped N–TiO_2/ZrO_2 sample exhibits an average crystallite size of 24.43 nm, which progressively decreases with increasing Ni incorporation, reaching a minimum of 11.10 nm at 5 wt% Ni. This reduction can be attributed to lattice distortion induced by the partial substitution of Ti^{4+} with Ni^{2+} ions and the formation of Ni–O–Ti linkages, which hinder crystal growth and suppress grain coalescence [26,27]. The smaller crystallite size is expected to increase the specific surface area and the density of exposed active sites, thereby favoring enhanced photocatalytic activity. However, at higher Ni loading (7 wt%), the crystallite size slightly increases to 13.67 nm, suggesting that excessive dopant concentration may promote particle agglomeration or the formation of Ni-rich segregated domains, partially offsetting the grain growth inhibition effect.

In contrast, the crystallite size of tetragonal ZrO_2 calculated from the (101) reflection remains nearly constant (29.16–29.97 nm) across all Ni concentrations, indicating that the ZrO_2 phase is structurally stable and largely unaffected by Ni doping. This invariance suggests that ZrO_2 primarily acts as a robust support phase that maintains the structural integrity of the composite while facilitating interfacial charge transfer, which is beneficial for improved visible-light photocatalytic performance [28].

3.2. Fourier Transform Infrared Spectroscopy

The FTIR spectra (Figure 3) further confirm the structural modifications induced by Ni and N dopants. The broad absorption bands at approximately 3440 cm^{-1} and 1620 cm^{-1} correspond to O–H stretching and bending

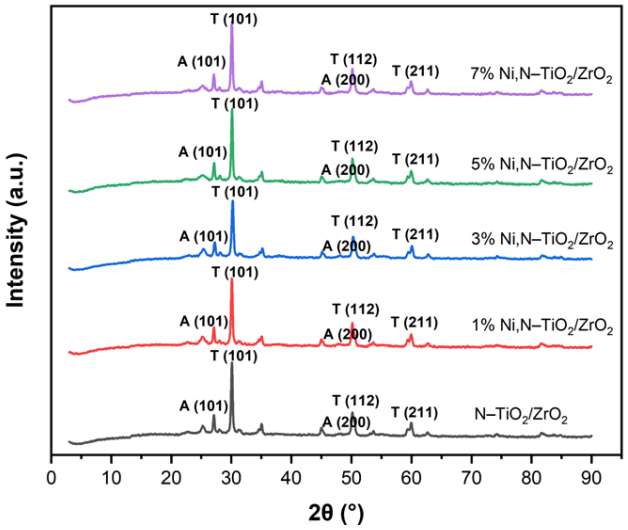

Figure 2. X-ray diffractograms of the synthesized photocatalysts.

Table 1. Crystallite size of the crystal phases in the synthesized photocatalysts.

Photocatalyst	Crystal phase	*hkl*	2θ (°)	FWHM (°)	*D* (nm)
N–TiO_2/ZrO_2	Tetragonal	101	30.06	0.2745	29.97
	Anatase	101	25.44	0.3334	24.43
1% Ni,N–TiO_2/ZrO_2	Tetragonal	101	30.07	0.2770	29.70
	Anatase	101	25.82	0.3400	23.97
3% Ni,N–TiO_2/ZrO_2	Tetragonal	101	30.00	0.2799	29.38
	Anatase	101	25.30	0.5510	14.78
5% Ni,N–TiO_2/ZrO_2	Tetragonal	101	30.06	0.2821	29.16
	Anatase	101	25.06	0.7334	11.10
7% Ni,N–TiO_2/ZrO_2	Tetragonal	101	30.09	0.2751	29.90
	Anatase	101	25.20	0.5956	13.67

vibrations, indicating the presence of surface hydroxyl groups and adsorbed water molecules. Urea served as the nitrogen precursor for doping. Upon calcination, urea thermally decomposes into NH_3 and isocyanic acid species, which subsequently generate reactive nitrogen intermediates capable of diffusing into the TiO_2 lattice. These intermediates favor substitutional or interstitial nitrogen incorporation, primarily forming Ti–O–N linkages rather than direct Ti–N bonds. The absorption band observed near 1111 cm^{-1} is therefore assigned to Ti–O–N stretching vibrations, which provides evidence for nitrogen incorporation into the TiO_2 framework and confirms successful N-doping [29].

A distinct band around 550 cm^{-1}, observed in all samples, is attributed to Zr–O or Ti–O stretching vibrations, characteristic of the TiO_2 and ZrO_2 frameworks. Ti–O–Ni vibrations are expected within the 400–750 cm^{-1} region, where they overlap with the intrinsic Ti–O and Zr–O modes. With increasing Ni concentration, the absorption bands in this region exhibit noticeable shifts and broadening, indicating enhanced lattice distortion, reduced crystallite size, and the formation of Ni–O–Ti linkages, which are consistent with the XRD results. At higher Ni loadings, these spectral changes become less distinct, likely due to Ni agglomeration or saturation of substitutional and interstitial sites within the TiO_2 lattice.

3.3. Optical Properties

The optical absorption properties (Figure 4) reveal a strong correlation between structural and electronic modifications induced by Ni–N co-doping. Analysis of the diffuse reflectance spectra shows that the absorption edge progressively shifts toward longer wavelengths (red shift) with increasing Ni content, reaching approximately 463 nm for the 5 wt% Ni sample. The bandgap energies were estimated by linear extrapolation of the absorption edge using a two-line intersection method, yielding a minimum value of 2.69 eV (Table 2). This reduction indicates significantly enhanced visible-light absorption.

The incorporation of Ni introduces localized 3d electronic states within the TiO_2 band structure, while nitrogen doping generates additional defect or O–Ti–N states near the valence band. The synergistic interaction of these dopants forms intermediate energy levels that effectively narrow the bandgap and facilitate electronic excitation under visible-light irradiation. These optical changes are consistent with the lattice distortion and new metal–oxygen/nitrogen bonding evidenced by the XRD and FTIR analyses.

For comparison, the pristine TiO_2/ZrO_2 composite prepared in this study exhibits a bandgap energy of 3.14 eV, slightly lower than the 3.25 eV reported for TiO_2/ZrO_2 systems by Shao *et al.* [30], suggesting effective interfacial interaction between TiO_2 and ZrO_2. Zhang *et al.* [31] reported a bandgap energy of 2.29 eV for Ni,N co-doped TiO_2 ($N(x)Ni(y)TiO_2$), demonstrating that simultaneous metal–nonmetal co-doping can substantially enhance visible-light absorption. The bandgap energy obtained in the present work (2.69 eV) is

Table 2. Bandgap energy of the synthesized photocatalysts.

Photocatalyst	Bandgap energy (eV)
N–TiO_2/ZrO_2	3.03
1% Ni,N–TiO_2/ZrO_2	2.99
3% Ni,N–TiO_2/ZrO_2	2.86
5% Ni,N–TiO_2/ZrO_2	2.69
7% Ni,N–TiO_2/ZrO_2	2.78

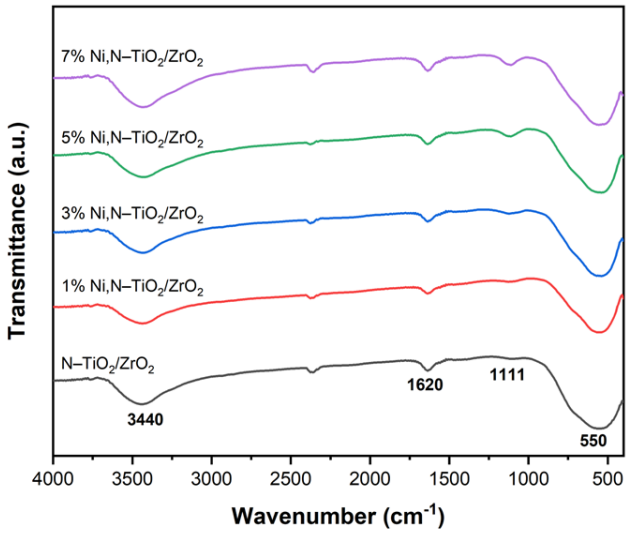

Figure 3. FTIR spectra of the synthesized photocatalysts.

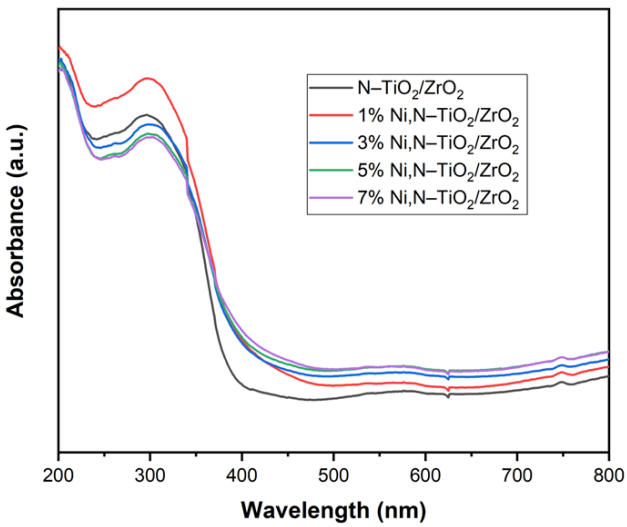

Figure 4. DRUV–Vis spectra of the synthesized photocatalysts.

comparable to those reported Ni,N-doped systems, confirming that Ni–N co-doping effectively tailors the electronic structure and extends light harvesting into the visible region while maintaining the structural stability of the TiO_2/ZrO_2 composite.

However, when the Ni content exceeds 5 wt%, the absorption edge shifts slightly toward shorter wavelengths (blue shift), and the bandgap energy increases to 2.78 eV at 7 wt%. This reversal is likely caused by excessive Ni promoting the formation of secondary phases or localized NiO clusters, which alter charge-carrier dynamics and partially counteract the beneficial bandgap-narrowing effect [32,33]. Altogether, the XRD, FTIR, and DRUV–Vis results demonstrate that moderate Ni co-doping (5 wt%) optimally modifies the structural, chemical, and optical properties of N–TiO_2/ZrO_2, enhancing visible-light absorption and photocatalytic potential without compromising crystallinity or phase stability.

3.4. Morphological and Surface Elemental Composition Analysis

The SEM micrograph of the 5% Ni,N–TiO_2/ZrO_2 photocatalyst (Figure 5) shows densely packed agglomerates consisting of nearly spherical nanoparticles, indicating uniform particle morphology. The EDX spectrum and elemental mapping confirm the even spatial distribution of Zr, Ti, O, N, and Ni throughout the sample, demonstrating homogeneous incorporation of the dopants within the TiO_2/ZrO_2 matrix without forming dopant-rich secondary phases.

This microstructural uniformity supports the XRD findings, which showed a single-phase crystalline structure with no additional peaks associated with Ni or N impurities. It is also consistent with the FTIR results, where subtle shifts in vibrational bands confirmed successful dopant substitution and lattice distortion. Furthermore, the homogeneous dispersion of the co-dopants is consistent with the DRUV–Vis findings, where bandgap narrowing and a red shift of the absorption edge were observed, suggesting synergistic electronic effects arising from the well-integrated Ni and N dopants. Collectively, these results confirm that Ni and N were effectively incorporated into the TiO_2/ZrO_2 framework, modifying its structural and electronic characteristics to enhance visible-light absorption and photocatalytic performance [34].

3.5. Photocatalytic Performance Evaluation of the Synthesized Photocatalysts

The photocatalytic activity of the synthesized Ni,N–TiO_2/ZrO_2 photocatalysts with varying Ni concentrations was systematically evaluated for phenol degradation under visible-light irradiation (Figure 6). All samples exhibited a continuous increase in phenol degradation efficiency with prolonged irradiation time. The degradation kinetics were analyzed using the Langmuir–Hinshelwood (L–H) model (Figure 7), which is commonly applied to heterogeneous photocatalytic reactions occurring on semiconductor surfaces, where the process involves adsorption of pollutant molecules followed by surface reaction [35,36]. Under the

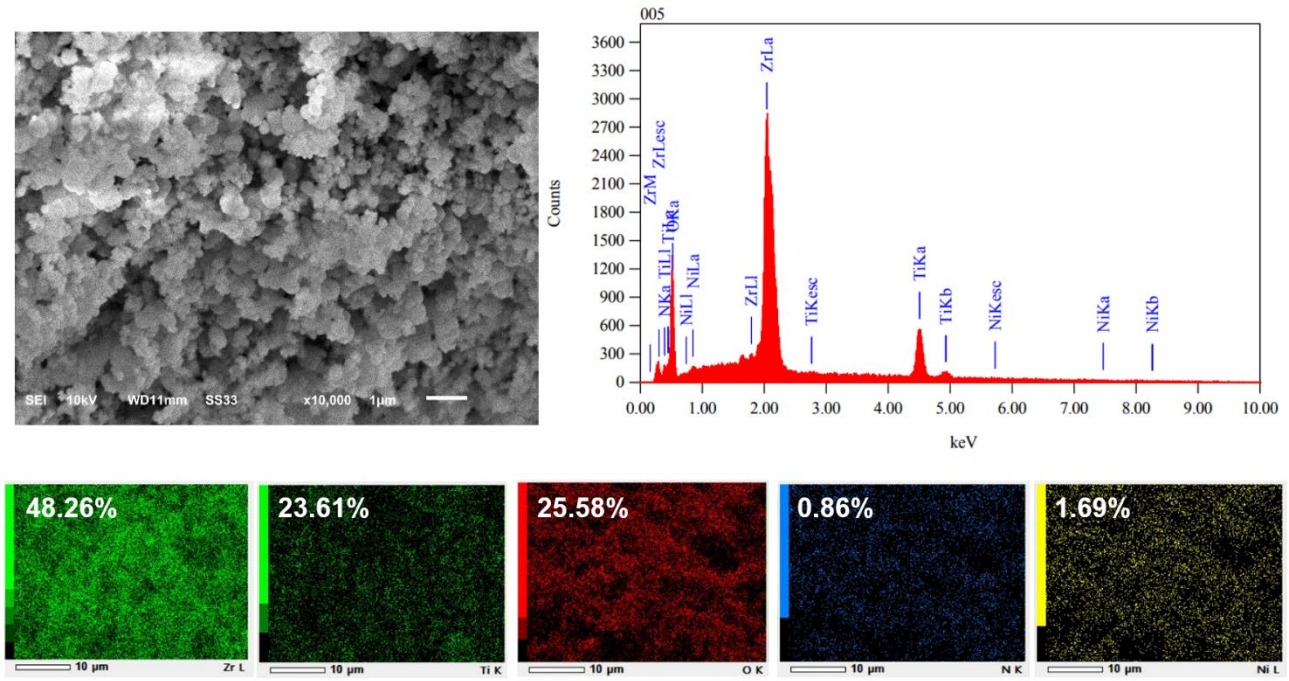

Figure 5. SEM–EDX mapping results of the 5% Ni,N–TiO_2/ZrO_2 photocatalyst (EDX results show the elemental composition in weight percentage).

relatively low initial phenol concentration used in this study (10 mg.L^{-1}), the L–H rate equation can be simplified to a pseudo-first-order form, expressed as ln (C_0/C) = kt. Therefore, the apparent rate constants (k) were obtained from the linear plots of ln (C_0/C) versus irradiation time.

As summarized in Table 3, the kinetic plots generally exhibited good linearity, with correlation coefficients (R^2) ranging from 0.86 to 0.999, supporting the applicability of the pseudo-first-order approximation. Slightly lower linearity observed for the low-activity sample (1 wt% Ni,N–TiO_2/ZrO_2, R^2 = 0.8596) is attributed to the limited phenol conversion and greater experimental fluctuations at small concentration changes. Both the apparent rate constant and degradation efficiency increased with Ni loading up to 5 wt%, at which the photocatalyst demonstrated the highest activity, achieving 85.36% removal and the largest rate constant (0.0229 min^{-1}, R^2 = 0.9992). Further increasing the Ni content to 7 wt% led to a decrease in activity, likely due to excessive dopant coverage and increased charge recombination, which reduced the number of accessible active sites.

The enhancement in photocatalytic performance at moderate Ni concentrations can be attributed to the synergistic effects of Ni and N dopants on the structural and electronic properties of the nanocomposite. As evidenced by the DRUV–Vis analysis, the incorporation of Ni introduced intermediate energy states within the TiO_2 band structure and effectively narrowed the bandgap, extending optical absorption into the visible-light region. This bandgap modification enables the photocatalyst to harness a greater portion of the solar spectrum, thereby increasing photon utilization efficiency. Furthermore, Ni^{2+} species can act as shallow electron traps that facilitate charge carrier separation and delay recombination, while nitrogen incorporation contributes to valence band modification through the mixing of N 2p and O 2p orbitals. These combined effects enhance the generation of reactive oxygen species (ROS), such as •OH and $•O_2^-$ radicals, which are the dominant oxidizing agents responsible for phenol degradation [37].

At higher Ni loadings (7 wt%), however, a noticeable decline in photocatalytic activity was observed. This deterioration is primarily attributed to the adverse effects of excessive dopant incorporation. As supported by XRD and FTIR analyses, excess Ni promotes lattice distortion and the possible formation of Ni-rich clusters, which can act as charge recombination

Table 3. Photocatalyst activity results for phenol degradation.

Photocatalyst	Phenol removal efficiency (%)	Rate constant (min^{-1})	R^2
N–TiO_2/ZrO_2	40.72	0.0042	0.9692
1% Ni,N–TiO_2/ZrO_2	41.98	0.0062	0.8596
3% Ni,N–TiO_2/ZrO_2	71.02	0.0136	0.9907
5% Ni,N–TiO_2/ZrO_2	85.36	0.0229	0.9992
7% Ni,N–TiO_2/ZrO_2	62.16	0.0102	0.9617

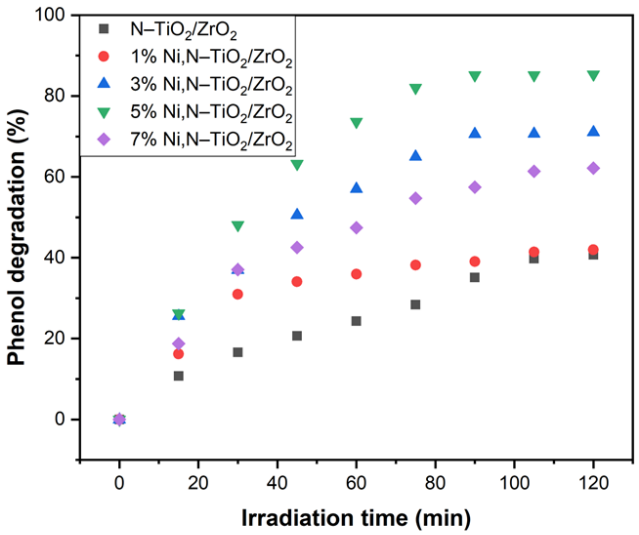

Figure 6. Phenol photodegradation results using the synthesized photocatalysts. Experimental conditions: initial phenol concentration = 10 mg.L^{-1} and photocatalyst mass = 100 mg.

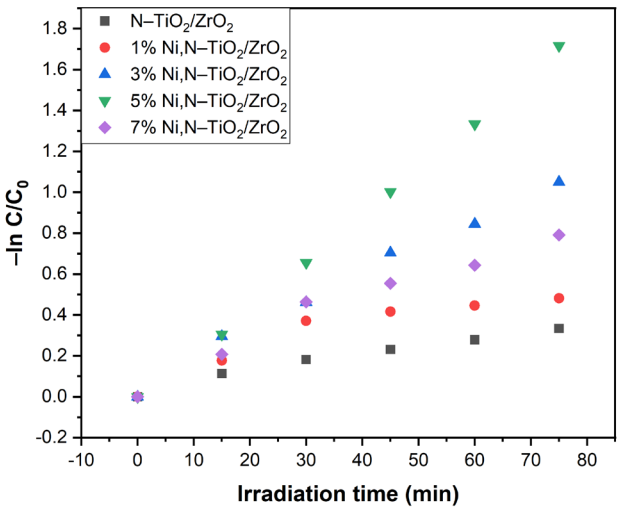

Figure 7. Langmuir–Hinshelwood kinetic model plots for phenol photodegradation using the synthesized photocatalysts. Experimental conditions: initial phenol concentration = 10 mg.L^{-1} and photocatalyst dosage = 100 mg.

centers that hinder electron–hole migration. The SEM–EDX mapping further indicated that, while Ni and N were homogeneously distributed at the optimal loading, excessive Ni may lead to partial aggregation and compositional inhomogeneity. Such agglomeration can limit light absorption uniformity and impede active site accessibility. Moreover, an excessive dopant concentration may induce electronic saturation within the TiO_2 lattice, disrupting the delicate balance between charge separation and recombination dynamics.

Comparable trends have been reported for other transition metal–doped oxide photocatalysts, where moderate dopant incorporation enhances photoactivity, but excessive doping results in recombination-dominated processes and reduced efficiency [38,39]. Overall, the findings suggest that an optimal Ni co-doping level of 5 wt% achieves a balance between structural stability, efficient charge separation, and extended visible-light response, leading to superior photocatalytic degradation performance of phenol.

3.6. Plausible Photocatalytic Mechanism, Comparison with Previous Studies, and Future Outlook

The plausible mechanism for phenol degradation over the Ni,N–TiO_2/ZrO_2 photocatalyst under visible-light irradiation is illustrated in Figure 8. When exposed to photons with energy equal to or greater than the narrowed bandgap (2.69 eV for 5 wt% Ni co-doping), electrons (e^-) are excited from the valence band (VB) to the conduction band (CB), generating electron–hole (h^+) pairs, as expressed in Equation (5):

$$\text{Ni,N–TiO}_2/\text{ZrO}_2 + h\nu \rightarrow e_{CB}^- + h_{VB}^+ \quad (5)$$

The synergistic co-doping of Ni and N introduces intermediate energy levels between the VB and CB, as supported by the DRUV–Vis, XRD, and FTIR results. These localized states extend the optical absorption of TiO_2 into the visible region while acting as shallow traps that inhibit the rapid recombination of photoexcited e^-–h^+ pairs.

The photogenerated electrons in the CB of Ni,N–TiO_2, are efficiently transferred to the CB of ZrO_2 due to the favorable band alignment between the two semiconductors, forming a heterojunction that promotes directional charge migration. The transferred electrons subsequently react with dissolved oxygen molecules to produce superoxide radicals ($\cdot O_2^-$), as shown in Equation (6):

$$O_2 + e_{CB}^- \rightarrow \cdot O_2^- \quad (6)$$

These reactive $\cdot O_2^-$ radicals can further undergo redox reactions, generating hydroxyl radicals ($\cdot$OH), either through the reduction of water molecules or hydroxide ions, as represented in Equations (7) and (8):

$$H_2O + h_{VB}^+ \rightarrow \cdot OH + H^+ \quad (7)$$
$$OH^- + h_{VB}^+ \rightarrow \cdot OH \quad (8)$$

Both $\cdot O_2^-$ and $\cdot$OH radicals possess high oxidative potential and play dominant roles in the photocatalytic degradation of phenol. These species attack phenol molecules adsorbed on the photocatalyst surface, initiating a sequence of oxidative reactions that break the aromatic ring and eventually mineralize the intermediates into CO_2 and H_2O, as described in Equation (9):

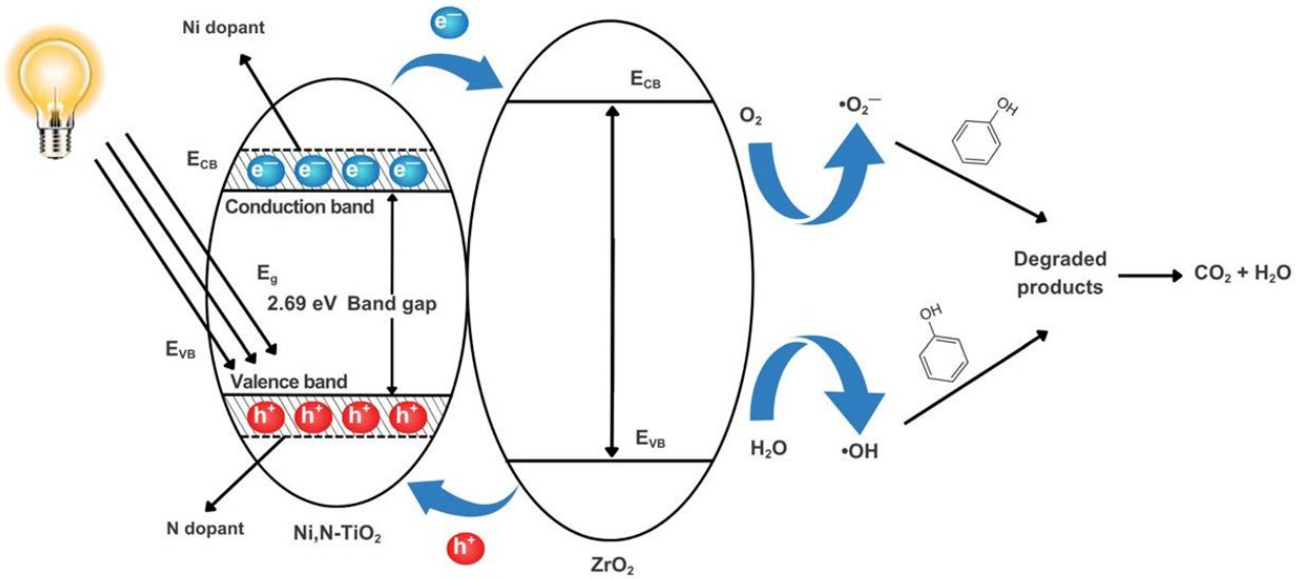

Figure 8. Proposed schematic mechanism for phenol degradation using the 5% Ni,N–TiO_2/ZrO_2 photocatalyst under visible-light irradiation.

$$Phenol + (\cdot OH, \cdot O_2^-) \rightarrow Degraded\ Products \rightarrow CO_2 + H_2O \quad (9)$$

The overall process involves the synergistic participation of Ni and N dopants, which enhance visible-light harvesting, improve charge separation, and facilitate radical generation. Ni^{2+} species act as electron traps that prolong the lifetime of charge carriers, while nitrogen doping contributes to valence band modification via N 2p–O 2p orbital hybridization. These effects collectively enhance photocatalytic efficiency by promoting efficient reactive oxygen species (ROS) formation and suppressing electron–hole recombination [40,41].

As summarized in Table 4, the 5% Ni,N–TiO_2/ZrO_2 photocatalyst achieved 85.36% phenol degradation under visible-light irradiation. This performance surpasses that of several reported visible-light photocatalysts, including Fe_3O_4/RGO (76.00%) under visible lamp irradiation, 5%C/TiO_2 (70.00%) under UV lamp irradiation, Fe/TiO_2–SiO_2 (~50.00%) under UV lamp irradiation, and ZnO–TiO_2/NCP (~20.00%) under visible lamp irradiation, and is comparable to Fe_3O_4@SiO_2 modified with silane agents (84.00%) under UV lamp irradiation. Although its efficiency is slightly lower than that of 30% TiO_2–montmorillonite (89.80%) under UV illumination, the present catalyst operates exclusively under visible light, representing a significant advantage for solar-driven applications.

The superior performance of the 5% Ni,N–TiO_2/ZrO_2 photocatalyst can be attributed to the synergistic effects of Ni and N dopants, which induce bandgap narrowing, enhance visible-light

Table 4. Comparison with other relevant studies conducted in recent years.

Photocatalyst	Operational conditions	Phenol removal efficiency (%)	Ref.
30%TiO_2/MMT	Phenol concentration = 10 mg.L^{-1}, solution volume = 100 mL, irradiation time = 240 min, photocatalyst dosage = 0.2 g, pH = 6, light source = UV lamp	89.80	[24]
5% Ni,N–TiO_2/ZrO_2	Phenol concentration = 10 mg.L^{-1}, solution volume = 100 mL, irradiation time = 2 h, photocatalyst dosage = 100 mg, light source = visible lamp	85.36	Present work
Fe_3O_4@SiO_2 mediated by silane agent	Phenol concentration = 50 mg.L^{-1}, solution volume = 350 mL, irradiation time = 9 h, photocatalyst dosage = 0.2 g, light source = UV lamp	84.00	[42]
SnO_2–TiO_2 (Sn/Ti = 1:2)	Phenol concentration = 10 mg.L^{-1}, solution volume = 25 mL, irradiation time = 2 h, photocatalyst dosage = 25 mg, light source = visible lamp	82.30	[43]
Fe_3O_4/RGO	Phenol concentration = 10 mg.L^{-1}, solution volume = 50 mL, irradiation time = 2 h, photocatalyst dosage = 50 mg, light source = visible lamp	76.00	[44]
5%C/TiO_2	Phenol concentration = 10 mg.L^{-1}, solution volume = 100 mL, irradiation time = 150 min, photocatalyst dosage = 0.2 g, light source = UV lamp	70.00	[23]
Fe/TiO_2–SiO_2	Phenol concentration = 50 mg.L^{-1}, solution volume = 50 mL, irradiation time = 2 h, photocatalyst dosage = 1 g.L^{-1}, pH = ~6.7, light source = UV lamp	~50.00	[22]
ZnO–TiO_2/NCP	Phenol concentration = not determined (wastewater containing phenol was used in this work), solution volume = 20 mL of 100-fold diluted wastewater, irradiation time = 300 min, photocatalyst dosage = 0.1 g.L^{-1}, pH = 3, light source = visible lamp	~20.00	[45]

absorption, and improve charge carrier separation [46]. Additionally, the incorporation of ZrO_2 contributes to stabilizing the anatase phase of TiO_2, preventing the anatase-to-rutile transformation and ensuring structural robustness during photocatalytic operation [47].

From a broader perspective, this study demonstrates the potential of Ni,N–TiO_2/ZrO_2 nanocomposites as efficient and sustainable visible-light-active photocatalysts for wastewater treatment. Nevertheless, the present work did not include the optimization of key operational parameters such as the initial phenol concentration, photocatalyst loading, and solution pH, all of which can significantly influence photocatalytic efficiency. These parameters will be systematically optimized in future studies to achieve a more comprehensive understanding of the catalytic behavior and reaction kinetics. Furthermore, detailed identification of degradation intermediates using a Liquid Chromatography–Mass Spectrometer (LC–MS) and other advanced spectroscopic techniques will be conducted to elucidate the phenol degradation pathway. Future efforts will also focus on refining synthesis parameters, tailoring surface morphology, and integrating the optimized photocatalyst into scalable photoreactor systems to enhance performance and enable real-world environmental remediation applications.

4. Conclusion

Nickel-modified nitrogen-doped titania/zirconia (Ni,N–TiO_2/ZrO_2) nanocomposites were successfully synthesized and demonstrated enhanced photocatalytic activity toward visible light-driven phenol degradation. The optimal composition containing 5 wt% Ni exhibited the highest performance, achieving 85.36% phenol removal with an apparent rate constant of 0.0229 min^{-1} after 120 min of irradiation. This enhanced activity is attributed to the synergistic interaction between Ni and N dopants, which effectively narrowed the band gap to 2.69 eV, improved charge carrier separation, and stabilized the anatase phase of TiO_2 against rutile transformation.

Taken together, this study confirms that dual metal–nonmetal doping serves as an efficient strategy to tailor the electronic structure and photocatalytic response of TiO_2/ZrO_2-based materials under visible light. Future investigations will focus on optimizing key operational parameters such as solution pH, catalyst dosage, and initial phenol concentration, as well as conducting radical scavenging tests, recyclability assessments, and long-term stability evaluations. The outcomes will provide a deeper understanding of the photocatalytic mechanism and facilitate the development of durable, visible-light-responsive photocatalysts for sustainable water purification applications.

Acknowledgment

This research was supported by the Lecturer Research Fund from the Faculty of Mathematics and Natural Sciences, Universitas Gadjah Mada under contract number 3938/UN1/FMIPA.1.3/KP/PT.01.03/2025. The authors also acknowledge the facilities and technical assistance provided by the Physical Chemistry Laboratory, Department of Chemistry, Universitas Gadjah Mada, which contributed to the successful completion of this research.

CRedit Author Statement

Author Contributions: A. Syoufian: Conceptualization, Project Administration, Resources, Supervision, Validation, Writing – Review and Editing. A.J. Saviola: Visualization, Validation, Writing – Original Draft. R.R. Janah: Methodology, Data Curation, Investigation. R. Afifah: Methodology, Data Curation, Investigation. K. Wijaya: Validation, Formal Analysis, Supervision, Writing – Review and Editing. R. Kurniawan: Validation, Formal Analysis, Supervision, Writing – Review and Editing. S. Sudiono: Validation, Formal Analysis, Supervision. W.-C. Oh: Validation, Formal Analysis, Supervision. W. Wangsa: Data Curation, Investigation. All authors have read and agreed to the published version of the manuscript.

References

[1] Lestari, D.Y., Wijaya, K., Syoufian, A., Hariani, P.L., Utami, M., Saviola, A.J., Fitria, R.A., Wahyuningsih, P., Bhagaskara, A., Wangsa, W., Chang, S.W., Ravindran, B. (2025). Unveiling the potency of graphene-based materials for water remediation: A brief review. *Journal of Molecular Structure*, 1335, 142018. DOI: 10.1016/j.molstruc.2025.142018.

[2] Bibi, A., Bibi, S., Abu-Dieyeh, M., Al-Ghouti, M.A. (2023). Towards sustainable physicochemical and biological techniques for the remediation of phenol from wastewater: A review on current applications and removal mechanisms. *Journal of Cleaner Production*, 417, 137810. DOI: 10.1016/j.jclepro.2023.137810.

[3] Wijaya, K., Bhagaskara, A., Sani, M.F.M., Vebryana, M.F., Pratama, F.A., Anggraeni, W., Amin, A.K., Ramadhani, F.A., Saviola, A.J. (2024). Sonochemically modified Lapindo mud using sulfuric acid for efficient adsorption of phenol in aqueous media and real wastewater samples. *Bulletin of Chemical Reaction Engineering & Catalysis*, 19, 635–648. DOI: 10.9767/bcrec.20228.

[4] Alshabib, M., Onaizi, S.A. (2019). A review on phenolic wastewater remediation using homogeneous and heterogeneous enzymatic processes: Current status and potential challenges. *Separation and Purification Technology*, 219, 186–207. DOI: 10.1016/j.seppur.2019.03.028.

[5] Said, K.A.M., Ismail, A.F., Karim, Z.A., Abdullah, M.S., Hafeez, A. (2021). A review of technologies for the phenolic compounds recovery and phenol removal from wastewater. *Process Safety and Environmental Protection*, 151, 257–289. DOI: 10.1016/j.psep.2021.05.015.

[6] Villegas, L.G.C., Mashhadi, N., Chen, M., Mukherjee, D., Taylor, K.E., Biswas, N. (2016). A short review of techniques for phenol removal from wastewater. *Current Pollution Reports*, 2, 157–167. DOI: 10.1007/s40726-016-0035-3.

[7] Garg, S., Kumar, P., Singh, S., Yadav, A., Dumée, L.F., Sharma, R.S., Mishra, V. (2020). *Prosopis juliflora* peroxidases for phenol remediation from industrial wastewater—An innovative practice for environmental sustainability. *Environmental Technology & Innovation*, 19, 100865. DOI: 10.1016/j.eti.2020.100865.

[8] Saravanan, A., Kumar, P.S., Jeevanantham, S., Karishma, S., Tajsabreen, B., Yaashikaa, P.R., Reshma, B. (2021). Effective water/wastewater treatment methodologies for toxic pollutants removal: Processes and applications towards sustainable development. *Chemosphere*, 280, 130595. DOI: 10.1016/j.chemosphere.2021.130595.

[9] Basaleh, A., Ismail, A.A., Mohamed, R.M. (2022). Novel visible light heterojunction CdS/Gd_2O_3 nanocomposite photocatalysts for Cr(VI) photoreduction. *Journal of Alloys and Compounds*, 927, 166988. DOI: 10.1016/j.jallcom.2022.166988.

[10] Utami, M., Wang, S., Musawwa, M.M., Mafruhah, L., Fitri, M., Wijaya, K., Johnravindar, D., Abd-Elkader, O.H., Yadav, K.K., Ravindran, B., Chung, W.J., Chang, S.W., Munusamy-Ramanujam, G. (2023). Photocatalytic degradation of naphthol blue from batik wastewater using functionalized TiO_2-based composites. *Chemosphere*, 337, 139224. DOI: 10.1016/j.chemosphere.2023.139224.

[11] Liang, S., Chen, Y., Han, W., Jiao, Y., Li, W., Tian, G. (2022). Hierarchical S-scheme titanium dioxide@cobalt–nickel based metal–organic framework nanotube photocatalyst for selective carbon dioxide photoreduction to methane. *Journal of Colloid and Interface Science*, 630, 11–22. DOI: 10.1016/j.jcis.2022.09.115.

[12] Utami, M., Rahmadhani, L.S., Wijaya, K., Ravindran, B., Alam, M.W., Hauli, L., Rianjanu, A., Purnama, I., Purwiandono, G. (2024). High effectiveness self-cleaning activity on TiO_2/rGO nanocomposite synthesized by mangosteen (*Garcinia mangostana* L.) peel extract. *Results in Engineering*, 24, 103593. DOI: 10.1016/j.rineng.2024.103593.

[13] Hu, Q., Huang, J., Li, G., Jiang, Y., Lan, H., Guo, W., Cao, Y. (2016). Origin of the improved photocatalytic activity of Cu incorporated TiO_2 for hydrogen generation from water. *Applied Surface Science*, 382, 170–177. DOI: 10.1016/j.apsusc.2016.04.126.

[14] Bashirom, N., Tan, W.K., Kawamura, G., Matsuda, A., Lockman, Z. (2022). Formation of self-organized ZrO_2–TiO_2 and $ZrTiO_4$–TiO_2 nanotube arrays by anodization of Ti–40Zr foil for Cr(VI) removal. *Journal of Materials Research and Technology*, 19, 2991–3003. DOI: 10.1016/j.jmrt.2022.06.055.

[15] Fazaeli, R., Aliyan, H., Nezamzadeh-Ejhieh, A., Richeson, D. (2024). Investigation of the synergistic photocatalytic activity of a ternary $ZrTiO_4/TiO_2/Mn_3O_4$ (ZTM) nanocomposite in a typical water treatment process. *Surface Innovations*, 52, 104877. DOI: 10.1016/j.surfin.2024.104877.

[16] Badli, N.A., Ali, R., Bakar, W.A.W.A., Yuliati, L. (2017). Role of heterojunction $ZrTiO_4/ZrTi_2O_6/TiO_2$ photocatalyst towards the degradation of paraquat dichloride and optimization study by Box–Behnken design. *Arabian Journal of Chemistry*, 10, 935–943. DOI: 10.1016/j.arabjc.2016.02.011.

[17] Andita, K.R., Kurniawan, R., Syoufian, A. (2019). Synthesis and characterization of Cu-doped zirconium titanate as a potential visible-light responsive photocatalyst. *Indonesian Journal of Chemistry*, 19, 761–766. DOI: 10.22146/ijc.39778.

[18] Cheng, X., Yu, X., Xing, Z., Yang, L. (2016). Synthesis and characterization of N-doped TiO_2 and its enhanced visible-light photocatalytic activity. *Arabian Journal of Chemistry*, 9, S1706–S1711. DOI: 10.1016/j.arabjc.2012.04.052.

[19] Lim, D.-H., Maitlo, H.A., Younis, S.A., Kim, K.-H. (2024). The practical utility of nitrogen-doped TiO_2 as a photocatalyst for the oxidative removal of gaseous formaldehyde. *Materials Today Nano*, 27, 100499. DOI: 10.1016/j.mtnano.2024.100499.

[20] Ahmed, W., Iqbal, J. (2021). Effect of Ni doping on structural, optical, and magnetic characteristics of ZrO_2 nanoparticles with efficient visible-light-driven photocatalytic activity. *Ceramics International*, 47, 24895–24095. DOI: 10.1016/j.ceramint.2021.05.216.

[21] Rajaramanan, T., Kumara, G.R.A., Velauthapillai, D., Ravirajan, P., Senthilnanthanan, M. (2021). Ni/N co-doped P25 TiO_2 photoelectrodes for efficient dye-sensitized solar cells. *Materials Science in Semiconductor Processing*, 135, 106062. DOI: 10.1016/j.mssp.2021.106062.

[22] Fuentes, K.M., Betancourt, P., Marrero, S., Garcia, S. (2017). Photocatalytic degradation of phenol using doped titania supported on photonic SiO_2 spheres. *Reaction Kinetics, Mechanisms and Catalysis*, 120, 403–415. DOI: 10.1007/s11144-016-1097-3.

[23] Zhang, J., Zheng, Y., Ma, M., Li, H. (2020). Structural characterization and photocatalytic activity of synthesized carbon-modified TiO_2 for phenol degradation. *Journal of Wuhan University of Technology – Materials Science Edition*, 35, 535–540. DOI: 10.1007/s11595-020-2290-9.

[24] Li, H., Yao, Y., Yang, X., Zhou, X., Lei, R., He, S. (2022). Degradation of phenol by photocatalysis using TiO_2/montmorillonite composites under UV light. *Environmental Science and Pollution Research*, 29, 68293–68305. DOI: 10.1007/s11356-022-20638-8.

[25] Jadhav, P.S., Jadhav, T., Bhosale, M., Jadhav, C.H., Pawar, V.C. (2021). Structural and optical properties of N-doped TiO_2 nanomaterials. *Materials Today: Proceedings*, 43, 2763–2767. DOI: 10.1016/j.matpr.2020.07.164.

[26] Elahifard, M.R., Ahmadvand, S., Mirzanejad, A. (2018). Effects of Ni-doping on the photocatalytic activity of TiO_2 anatase and rutile: Simulation and experiment. *Materials Science in Semiconductor Processing*, 84, 10–16. DOI: 10.1016/j.mssp.2018.05.001.

[27] Alijani, M., Ilkhechi, N.N. (2018). Effect of Ni doping on the structural and optical properties of TiO_2 nanoparticles at various concentration and temperature. *Silicon*, 10, 2569–2575. DOI: 10.1007/s12633-018-9792-5.

[28] Saviola, A.J., Syoufian, A., Oh, W.-C., Wijaya, K. (2025). Atmospheric hydrotreatment of used palm cooking oil over nickel-dispersed phosphated zirconia as highly stable nano-catalyst for bio-jet fuel production. *Inorganic Chemistry Communications*, 173, 113790. DOI: 10.1016/j.inoche.2024.113790.

[29] Shinde, S.G., Patil, M.P., Kim, G.-D., Shrivastava, V.S. (2020). Ni, C, N, S multi-doped ZrO_2 decorated on multi-walled carbon nanotubes for effective solar-induced degradation of anionic dye. *Journal of Environmental Chemical Engineering*, 8, 103769. DOI: 10.1016/j.jece.2020.103769.

[30] Shao, G.N., Imran, S.M., Jeon, S.J., Engole, M., Abbas, N., Haider, M.S., Kang, S.J., Kim, H.T. (2014). Sol–gel synthesis of photoactive zirconia–titania from metal salts and investigation of their photocatalytic properties in the photodegradation of methylene blue. *Powder Technology*, 258, 99–109. DOI: 10.1016/j.powtec.2014.03.024.

[31] Zhang, X., Liu, Q. (2008). Visible-light-induced degradation of formaldehyde over titania photocatalyst co-doped with nitrogen and nickel. *Applied Surface Science*, 254, 4780–4785. DOI: 10.1016/j.apsusc.2008.01.094.

[32] Baruah, M., Ezung, S.L., Sharma, S., Sinha, U.B., Sinha, D. (2022). Synthesis and characterization of Ni-doped TiO_2 activated carbon nanocomposite for the photocatalytic degradation of anthracene. *Inorganic Chemistry Communications*, 144, 109905. DOI: 10.1016/j.inoche.2022.109905.

[33] Syerk, K., Wierzbicka, E., Zych, M., Piecha, D., Szczerba, M., Sołtys-Mroz, M., Kapusta-Kołodziej, J., Sulka, G.D. (2025). Band gap engineering of tungsten oxide-based nanomaterials. *Journal of Photochemistry and Photobiology C: Photochemistry Reviews*, 62, 100681. DOI: 10.1016/j.jphotochemrev.2024.100681.

[34] Deng, P., Gan, M., Zhang, X., Li, Z., Hou, Y. (2019). Non-noble-metal Ni nanoparticles modified N-doped g-C_3N_4 for efficient photocatalytic hydrogen evolution. *International Journal of Hydrogen Energy*, 44, 30084–30092. DOI: 10.1016/j.ijhydene.2019.09.129.

[35] Khuzwayo, Z., Chirwa, E.M.N. (2017). Analysis of catalyst photo-oxidation selectivity in the degradation of polyorganochlorinated pollutants in batch systems using UV and UV/TiO_2. *South African Journal of Chemical Engineering*, 23, 17–25. DOI: 10.1016/j.sajce.2016.12.002.

[36] Rezaei, M., Ensafi, A.A. (2025). TiO_{2-x}-MoS_2 heterostructure: A study of kinetic, thermodynamic, and scavenging agents' effects in photodegradation. *Materials Science in Semiconductor Processing*, 188, 109162. DOI: 10.1016/j.mssp.2024.109162.

[37] Chen, K., Dong, W., Huang, Y., Wang, F., Zhou, J.L., Li, W. (2025). Photocatalysis for sustainable energy and environmental protection in construction: A review on surface engineering and emerging synthesis. *Journal of Environmental Chemical Engineering*, 13, 117529. DOI: 10.1016/j.jece.2025.117529.

[38] Santos, E., Catto, A.C., Peterline, A.F., Jr, W.A. (2022). Transition metal (Nb and W) doped TiO_2 nanostructures: The role of metal doping in their photocatalytic activity and ozone gas-sensing performance. *Applied Surface Science*, 579, 152146. DOI: 10.1016/j.apsusc.2021.152146.

[39] Maran, M.A., Zheng, A.L.T., Tan, H.Y., Sarbini, S.R., Tan, K.B., Boonyuen, S., Wong, K.K.S., Chung, E.L.T., Llease, J., Andou, Y. (2025). Assessing the photocatalytic performance of hydrothermally synthesized Fe-doped $BiVO_4$ under low-intensity UV irradiation. *Arabian Journal for Science and Engineering*. DOI: 10.1007/s13369-025-10278-8.

[40] Liu, Y., Zhu, Y., Xu, J., Bai, X., Zong, R., Zhu, Y. (2013). Degradation and mineralization mechanism of phenol by $BiPO_4$ photocatalysis assisted with H_2O_2. *Applied Catalysis B: Environmental*, 142–143, 561–567. DOI: 10.1016/j.apcatb.2013.05.049.

[41] Grosu, E.F., Cârjă, G., Froidevaux, R. (2018). Development of horseradish peroxidase/layered double hydroxide hybrid catalysis for phenol degradation. *Research on Chemical Intermediates*, 44, 7731–7752. DOI: 10.1007/s11164-018-3583-x.

[42] Rehman, G.U., Tahir, M., Goh, P.S., Ismail, A.F., Hafeez, A., Khan, I.U. (2021). Enhancing the photodegradation of phenol using Fe_3O_4/SiO_2 binary nanocomposite mediated by silane agent. *Journal of Physics and Chemistry of Solids*, 153, 110022. DOI: 10.1016/j.jpcs.2021.110022.

[43] Yang, J., Zhang, J., Zou, B., Zhang, H., Wang, J., Schubert, U., Rui, Y. (2020). Black SnO_2–TiO_2 nanocomposites with high dispersion for photocatalytic and photovoltaic applications. *ACS Applied Nano Materials*, 3, 4265–4273. DOI: 10.1021/acsanm.0c00432.

[44] Padhi, D.K., Panigrahi, T.K., Parida, K., Singh, S.K., Mishra, P.M. (2017). Green synthesis of Fe_3O_4/RGO nanocomposite with enhanced photocatalytic performance for Cr(VI) reduction, phenol degradation, and antibacterial activity. *ACS Sustainable Chemistry & Engineering*, 5, 10551–10562. DOI: 10.1021/acssuschemeng.7b02548.

[45] Nezamzadeh-Ejhieh, A., Bahrami, M. (2015). Investigation of the photocatalytic activity of supported ZnO–TiO_2 on clinoptilolite nanoparticles towards photodegradation of wastewater-contained phenol. *Desalination and Water Treatment*, 55, 1096–1104. DOI: 10.1080/19443994.2014.922443.

[46] R.R. Janah, (2024) Remediation of Phenol Pollutants Under Visible Light Irradiation Using High Performance Photocatalyst Ni-N-Codoped $ZrTiO_4$, *Master Thesis*, Universitas Gadjah Mada (in Indonesian).

[47] R. Afifah, (2025) Synthesis of N-Co-codoped TiO_2 nanocomposite immobilized on ZrO_2 as a photocatalyst for photodegradation of malachite green under visible light irradiation, *Master Thesis*, Universitas Gadjah Mada (in Indonesian).